JOURNAL OF COMPUTATIONAL PHYSICS **127,** 398–411 (1996)
ARTICLE NO. 0183

A Large-Domain Approach for Calculating Ship Boundary Layers and Wakes and Wave Fields for Nonzero Froude Number

Y. TAHARA* AND F. STERN

Iowa Institute of Hydraulic Research, The University of Iowa, Iowa City, Iowa

Received September 12, 1995; revised March 11, 1996

A large-domain approach is developed for calculating ship boundary layers and wakes and wave fields for nonzero Froude number. The Reynolds-averaged Navier–Stokes and continuity equations are solved with the Baldwin–Lomax turbulence model, exact nonlinear kinematic and approximate dynamic free-surface boundary conditions, and a body/free-surface conforming grid. The results are validated through comparisons with data for the Series 60 $C_B = 0.6$ ship model at low and high Froude numbers and results of a precursory interactive approach. Both approaches yield satisfactory results; however, the large-domain results indicate improved resolution of the flow close to the hull and wake centerplane and of the Froude number differences due to near-wall turbulence modeling and nonlinear free-surface boundary conditions. Additional evaluation is provided through discussion of the recent CFD Workshop Tokyo 1994, where both methods were among the best. Last, some concluding remarks are made.

INTRODUCTION

There is a current need for the development and validation of computational fluid dynamics (CFD) methods for surface–ship boundary layers and wakes and wave fields in support of anticipated future designs. At present, both interactive and large-domain approaches for solving the Reynolds-averaged Navier–Stokes (RANS) equations are viable alternatives and need relative assessment. The former refers to interactively combining viscous- and inviscid-flow methods for the inner and outer regions, respectively, whereas the latter refers to using a viscous-flow method for the entire domain. The interactive approach has the advantages of both the inviscid- and viscous-flow methodologies and computational efficiency, but it is inherently limited by the inviscid-flow method. The large-domain approach has the advantages of ease of implementation, more general applicability (e.g., massively separated flows), and utility (e.g., inclusion of thermal stratification, two-fluid modeling, etc.) and the limitations solely due to Reynolds averaging and current pacesetting issues in the CFD development. Also, both approaches are subject to developments associated with the treatment of free-surface boundary conditions and effects. Here again, the large-domain approach has an advantage in the ability for inclusion of viscous and turbulence effects over the entire domain. Thus, the large-domain approach is ultimately superior in offering more general applicability and utility and the possibility of a more detailed resolution of the flow.

The authors have been involved in the development of both approaches. Initially, an interactive approach was developed and validated [1, 2]. Herein, modifications and extensions are made for a large-domain approach, including improved numerical algorithms, Baldwin–Lomax turbulence model, exact nonlinear kinematic and approximate dynamic free-surface boundary conditions, and a body/free-surface conforming grid. The results are validated through comparisons with data for the Series 60 $C_B = 0.6$ ship model at low and high Froude numbers ($Fr = U_0/\sqrt{gL}$) [3, 4], and the precursory interactive approach. The latter comparisons also enable a qualitative relative assessment of the two approaches. Cost and time constraints, as well as problem complexity, precluded a quantitative relative assessment as was possible previously for zero Fr [5]. The zero Fr solution refers to the treatment of the free surface as a symmetry plane (i.e., double-body solution) corresponding to a condition of infinite gravity. Additional evaluation is provided through discussion of the performance of both approaches at the recent *CFD Workshop, Tokyo 1994* [6], where both methods were among the best, along with a summary and conclusions from the workshop, which also serve as an update of the reviews of [1, 2].

In the following, a detailed overview of the computational method is provided. The conditions and grids are described. Then, the results are validated for $Fr = 0$ and 0.316 through comparisons with the data and the interactive approach. Next, the *CFD Workshop, Tokyo 1994* [6] is discussed. Last, some concluding remarks are made.

* Current address: Department of Marine System Engineering, College of Engineering, University of Osaka Prefecture, 1-1, Gakuen-cho, Sakai, Osaka 593, Japan.

0021-9991/96 $18.00

COMPUTATIONAL METHOD

As already noted, the computational method is based on modifications and extensions of the precursory interactive approach [1, 2]. Recently, Stern *et al.* [9] provided a detailed description of the method to aid in the transition for design applications, including extensions for naval combatants with bulbous bows and transom sterns, utilizing multiblock domain decomposition and propeller-hull interaction, utilizing the method of Stern *et al.* [10]. Herein, an overview is given. Note that the core viscous-flow solver is based on Chen and Patel [7, 8] which has been validated for a variety of benchmark cases and applications.

Equations, Coordinate Systems, and the Turbulence Model

The unsteady RANS and continuity equations for an incompressible fluid are written in nondimensional form and Cartesian tensor notation as

$$\frac{\partial U_i}{\partial x_i} = 0 \tag{1}$$

$$\frac{\partial U_i}{\partial t} + U_j \frac{\partial U_i}{\partial x_j} = -\frac{\partial \hat{p}}{\partial x_i} + \frac{1}{\mathrm{Re}} \frac{\partial^2 U_i}{\partial x_j \partial x_j} - \frac{\partial}{\partial x_j}(\overline{u_i u_j}), \tag{2}$$

where $U_i = (U, V, W)$ are the mean-velocity components, $x_i = (X, Y, Z)$ are the Cartesian coordinates, $\hat{p}$ is the piezometric pressure ($p + \rho g z$), $\overline{u_i u_j}$ are the Reynolds stresses, ν is the kinematic viscosity, and $\mathrm{Re} = U_o L/\nu$ is the Reynolds number. The Reynolds stresses are related to the mean rate of strain through an isotropic eddy viscosity ν_t,

$$-\overline{u_i u_j} = \nu_t \left(\frac{\partial U_i}{\partial x_j} + \frac{\partial U_j}{\partial x_i} \right) - \frac{2}{3} \delta_{ij} k, \tag{3}$$

where δ_{ij} is the Kronecker delta and k is the turbulent kinetic energy. The equations are normalized by reference velocity U_o and length L and density ρ. Closure is attained through the Baldwin–Lomax algebraic turbulence model without modifications for free-surface effects.

The equations are transformed into nonorthogonal curvilinear coordinates such that the computational domain forms a simple rectangular parallelepiped with equal grid spacing. The transformation is a partial one since it involves the coordinates, only, and not the velocity components U_i. The transformation is accomplished through use of the expression for the divergence and ''chain-rule'' definitions of the gradient and Laplacian operators which relate the Cartesian coordinates x_i to the nonorthogonal coordinates (ξ, η, ζ). In this manner, (1) and (2) with (3) can be written in the form

$$\frac{\partial U^i}{\partial \xi^i} = 0 \tag{4}$$

$$g^{ii} \frac{\partial^2 \phi}{\partial \xi^i \partial \xi^i} - 2 a_\phi^j \frac{\partial \phi}{\partial \xi^j} = R_{\mathrm{eff}} \frac{\partial \phi}{\partial \tau} + S_\phi, \tag{5}$$

where U^i are the modified contravariant velocity components in the direction of the transformed coordinates, $\phi = (U, V, W)$, R_{eff} is an effective Reynolds number ($1/R_{\mathrm{eff}} = 1/\mathrm{Re} + \nu_t$), S_ϕ are source terms, τ is the computational time, and the geometric coefficients b_i^j, g^{ii}, and Jacobian J are functions of the coordinates only.

Discretization and Pressure Equation

Equation (5) is reduced to algebraic form through the use of the finite-analytic method. Solution-dependent coefficients are analytically derived by solving the linearized momentum equation on a computational cell with dimensions $21 \times 2k \times 2h$ using a hybrid method which combines a two-dimensional analytic solution in the $\eta\zeta$-plane with a one-dimensional analytic solution in the ξ-direction. By specifying boundary conditions on the faces of the cell as a combination of exponential and linear functions, which are the natural solutions for the linearized momentum equation, (5) can be solved by the method of separation of variables. When the solution is evaluated at the center node P (i.e., (i, j, k)) of the element, the following 12-point finite analytic formula is obtained,

$$\begin{aligned} \phi_P^n = \frac{1}{1 + C_P(C_U + C_D + R_{\mathrm{eff}}/\Delta\tau)} [& C_{NE}\phi_{NE}^n + C_{NW}\phi_{NW}^n \\ & + C_{SE}\phi_{SE}^n + C_{SW}\phi_{SW}^n + C_{EC}\phi_{EC}^n + C_{WC}\phi_{WC}^n \\ & + C_{NC}\phi_{NC}^n + C_{SC}\phi_{SC}^n + C_P(C_U\phi_U + C_D\phi_D \\ & + R_{\mathrm{eff}}\phi_P^{n-1}/\Delta\tau - (S_\phi)_P)], \end{aligned} \tag{6}$$

where C_{nb} ($nb = NE, NW$, etc.), C_P, C_U, and C_D are the finite-analytic coefficients and the subscripts P, U, and D denote the center, upstream, and downstream nodes, respectively, and NC, NW, WC, etc. denote the nodes in the $\eta\zeta$-plane in terms of compass directions. The superscripts (n) and $(n-1)$ refer to the current and previous time levels and $\Delta\tau$ is the time step. It is seen that ϕ_p depends on all eight neighboring nodal values in the transverse plane, as well as the values at the upstream and downstream nodes ϕ_U and ϕ_D and the values at the previous time step ϕ_P^{n-1}. The pressure-gradient and cross-derivative terms in $(S_\phi)_P$ are evaluated using second-order central finite differences. A regular-grid (i.e., variable-collocated) approach is used such that (6) is evaluated at P for $\phi = U$, V, and W.

The use of a regular grid results in the problem of odd–even decoupling of the pressure and velocity fields. There-

fore, the derivation of the pressure equation requires special treatment to eliminate this problem. The pressure equation is derived using the generalized continuity equation (4) in discrete form and a staggered-grid control volume. Discretizing (4) on this control volume using second-order central finite differences, decomposing the modified contravariant velocity into pseudovelocity and pressure-gradient terms, and discretizing the pressure-gradient terms with second-order central finite differences about the staggered-grid locations results in

$$\begin{aligned}(E_d^{11} + E_u^{11} + E_n^{22} + E_s^{22} + E_e^{33} + E_w^{33})\hat{p}_P \\ = E_d^{11}\,\hat{p}_D + E_u^{11}\,\hat{p}_U + E_n^{22}\,\hat{p}_{NC} + E_s^{22}\,\hat{p}_{SC} \\ + E_e^{33}\,\hat{p}_{EC} + E_w^{33}\,\hat{p}_{WC} - \hat{D},\end{aligned} \tag{7}$$

where E^{ij} and $\hat{D}$ are the pressure coefficients and mass source, respectively, and are defined as

$$E^{ij} = \frac{R_{\text{eff}} C_P}{J[1 + C_P(C_U + C_D + R_{\text{eff}}/\Delta\tau)]}\, b^i_m b^j_m \tag{8}$$

$$\hat{D} = \hat{U}^1_d - \hat{U}^1_u + \hat{U}^2_n - \hat{U}^2_s + \hat{U}^3_e - \hat{U}^3_w, \tag{9}$$

where $\hat{U}^i$ is a modified contravariant pseudovelocity field which contains part of the pressure-gradient if the grid is nonorthogonal. Since (7) is in terms of E^{ij} and $\hat{D}$ at the staggered-grid locations, one-dimensional linear interpolation is used to obtain both of these quantities at the staggered nodes, but in terms of the values calculated at the regular-grid locations.

Boundary Conditions and Grid Generation

Referring to Fig. 1, the specified boundaries of the solution domain are the body surface S_b, the inlet plane S_i, the exit plane S_e, the symmetry plane S_k, the outer boundary S_o, and the free-surface S_ζ. Note that for zero Fr, S_ζ becomes the waterplane S_w.

For zero Fr the boundary conditions are as follows: on S_b, $\phi = \partial p/\partial n = 0$ (where n is normal to the body); on S_i, free-stream values are imposed, i.e., $U = U_0$, $V = W = p = 0$; on S_e, a zero gradient condition is used, i.e., $\partial(\phi, p)/\partial X = 0$; on S_k and S_w, $\partial(U, W, p)/\partial Y = V = 0$ and $\partial(U, V, p)/\partial Z = W = 0$, respectively; and on S_o, $U = U_0$, $V = \partial p/\partial r = 0$ (where r is the radial coordinate), and W is extrapolated.

For nonzero Fr, the boundary conditions are similar, except: p is replaced by $\hat{p}$; and on S_ζ, exact nonlinear kinematic and approximate dynamic free-surface conditions are applied on the actual free surface, which is determined as part of the solution. The derivation of these conditions and the procedure for determining the free surface are described next.

On the free surface, there are two boundary conditions. The kinematic condition requires that ζ is a stream surface:

$$\frac{DF}{Dt} = 0, \quad F = \zeta - z. \tag{10}$$

The dynamic condition requires that the normal and tangential stresses are continuous across the surface,

$$\tau_{ij} n_j = \tau^*_{ij} n_j, \tag{11}$$

where n_j is the unit normal vector to the free surface and τ_{ij} $(= -p\delta_{ij} + \text{Re}^{-1}(\partial U_i/\partial x_j + \partial U_j/\partial x_i) - \overline{u_i u_j})$ and τ^*_{ij} are the fluid- and external-stress tensors, respectively. The latter includes surface tension. The following approximations were made in employing (11): (a) the external stress and surface tension are assumed to be zero; (b) the curvature of the free surface and gradients of the normal velocity component are assumed small. Expansion of (10) and reduction of (11) results in

$$\frac{\partial \zeta}{\partial t} + \tilde{U}\frac{\partial \zeta}{\partial \xi} + \tilde{V}\frac{\partial \zeta}{\partial \eta} - W = 0, \tag{12}$$

where

$$\tilde{U} = \frac{1}{J}(b^1_1 U + b^1_2 V)$$

$$\tilde{V} = \frac{1}{J}(b^2_1 U + b^2_2 V)$$

$$\hat{p} = \frac{\zeta}{\text{Fr}^2} \tag{13}$$

$$\frac{\partial(U, V)}{\partial z} = 0. \tag{14}$$

Last, a zero-gradient condition is used for W, which is consistent with the approximations employed for the dynamic condition,

$$\frac{\partial W}{\partial z} = 0. \tag{15}$$

Note that the pressure boundary condition (13) is inviscid in that it can be obtained directly by neglecting the normal viscous stress.

These conditions were implemented as follows: (13)–(15) are used as boundary conditions for the pressure and velocity; Eq. (12) is used to solve for the free-surface ζ iteratively, in conjunction with the global iteration procedure. For each global iteration, (12) is solved, whereupon the computational grid is regenerated so that it conforms

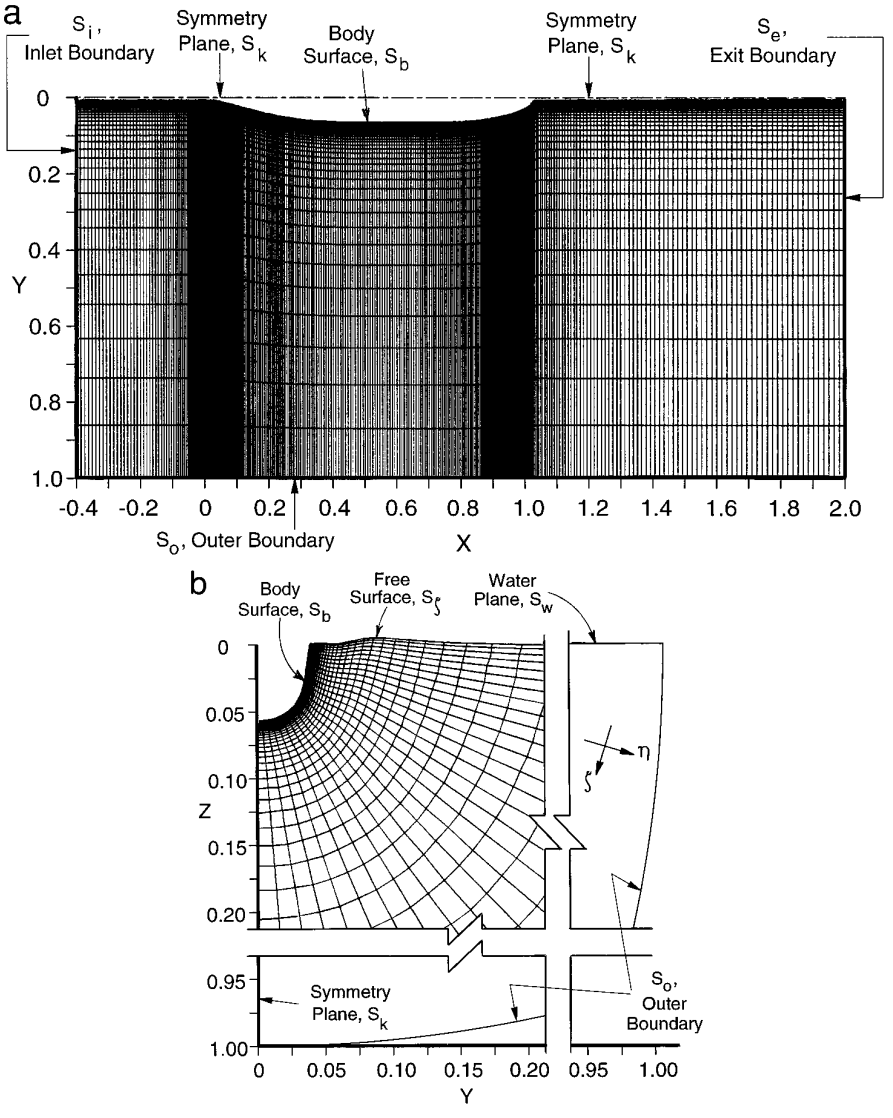

FIG. 1. Solution domain and computational grid: (a) Longitudinal plane; (b) Body crossplane.

to both the body and the free-surface. The procedure for solving (12) and adjusting the grid is outlined next.

Equation (12) is solved using a Beam and Warming linear-multistep method based upon space-centered finite-differences, approximate factorization, and the addition of both implicit and explicit fourth-order artificial dissipation. The temporal derivative is expressed as

$$\zeta^{n+1} = \zeta^n + \frac{\Delta t}{2}[(\zeta_t)^n + (\zeta_t)^{n+1}] \tag{16}$$

or

$$\zeta^{n+1} = \zeta^n - \frac{\Delta t}{2}[(\tilde{U}\zeta_\xi + \tilde{V}\zeta_\eta - W)^n + (\tilde{U}\zeta_\xi + \tilde{V}\zeta_\eta - W)^{n+1}]. \tag{17}$$

Introducing the delta form such that $\Delta\zeta^n = \zeta^{n+1} - \zeta^n$ and the differential operator L, (17) reduces to

$$L[\Delta\zeta^n] = \Delta t(W - \tilde{U}\zeta_\xi - \tilde{V}\zeta_\eta)^n, \tag{18}$$

where

$$L = \left\{1 + \frac{\Delta t}{2}\left(\frac{\partial}{\partial\xi}(\tilde{U})^n + \frac{\partial}{\partial\eta}(\tilde{V})^n\right)\right\}. \tag{19}$$

If L is factored into one-dimensional operators, L_1 and L_2, (18) becomes

$$L_1[\Delta\zeta^n] \cdot L_2[\Delta\zeta^n] = \Delta t(W - \tilde{U}\zeta_\xi - \tilde{V}\zeta_\eta)^n, \tag{20}$$

where

$$L_1 = \left\{1 + \frac{\Delta t}{2}\frac{\partial}{\partial \xi}(\tilde{U})^n\right\}$$
$$L_2 = \left\{1 + \frac{\Delta t}{2}\frac{\partial}{\partial \eta}(\tilde{V})^n\right\}. \quad (21)$$

Equation (20) can now be solved in two one-dimensional inversions

$$\textit{Step } 1.\ L_1[\Delta\zeta'] = \Delta t(W - \tilde{U}\zeta_\xi - \tilde{V}\zeta_\eta)^n \quad (22)$$
$$\textit{Step } 2.\ L_2[\Delta\zeta^n] = \Delta\zeta'. \quad (23)$$

Finally, the spatial derivatives in L_1 and L_2 are discretized using a second-order central difference and both implicit and explicit fourth-order artificial dissipation ε are added to damp out oscillations and/or maintain stability:

$$\textit{Step } 1.\ L_1^*[\Delta\zeta'] = \Delta t\Bigg(W - \tilde{U}\zeta_\xi - \tilde{V}\zeta_\eta - \varepsilon_\xi\frac{\partial^4\zeta}{\partial\xi^4} - \varepsilon_\eta\frac{\partial^4\zeta}{\partial\eta^4}\Bigg)^n \quad (24)$$
$$\textit{Step } 2.\ L_2^*[\Delta\zeta^n] = \Delta\zeta', \quad (25)$$

where

$$L_1^* = \left\{1 + \frac{\Delta t}{2}\frac{\partial}{\partial \xi}(\tilde{U})^n + \varepsilon_\xi\frac{\partial^4}{\partial\xi^4}\right\}$$
$$L_2^* = \left\{1 + \frac{\Delta t}{2}\frac{\partial}{\partial \eta}(\tilde{V})^n + \varepsilon_\eta\frac{\partial^4}{\partial\eta^4}\right\}. \quad (26)$$

The amount of artificial dissipation is $\varepsilon = 0.4$ and local time stepping is used with $\Delta t = 0.001(U^2 + V^2 + W^2)^{-1/2}$. Parametric studies indicate convergent solutions for $0.04 \le \varepsilon \le 4$. Smaller values produce checkerboard decoupling of the wave solution, whereas large values cause excessive wave damping. For each step in the approximate factorization (24) and (25), a pentadiagonal solver is used to determine the wave solution. Referring to Fig. 1, (12) is solved with boundary conditions: on the inlet boundary, $\Delta\zeta = 0$; on the exit boundary, $\Delta\zeta = ax^2 + c$; on the body and centerline boundaries, $\Delta\zeta = aY^2 + c$; and on the far-field boundary, $\partial(\Delta\zeta)/\partial Y = 0$. Finally, to accurately resolve both the wave and velocity fields, a method was developed to solve (12) using a two-dimensional grid generated separately from, but coupled to, the RANS grid. A simple procedure is used to facilitate the conforming of the RANS grid to both the hull and the free surface.

The RANS grid is H-type with constant-X planes stacked to form a complete three-dimensional grid. The bow and stern are resolved with axial clustering of grid points which are distributed using hyperbolic tangent stretching functions. Because of the H-type grid, non-vertical bows and sterns are resolved in a staircase fashion. The constant-X cross-plane grids are generated elliptically by solving a Poisson equation for the transformation between (Y, Z) and (η, ζ). Spacings are specified in the η-direction at the surface of the hull, which for the Baldwin–Lomax turbulence model should be at a $Y^+ \approx 1$, and in the ζ-direction at both the centerplane and free surface. The initial grid must extend to an elevation sufficiently above the zero, or design waterline, to allow for wave crests. As the wave field develops, the RANS grid conforms to the free surface. By confining the grid points and saving the initial distribution along η = const, or girth-wise lines, the grid is easily updated; the point on the free surface moves to a new elevation and all points below the free-surface slide along the η = const line so as to maintain the initial relative distribution.

The kinematic free-surface boundary condition (12) grid is two-dimensional (i.e., function of (X, Y)), updated iteratively to fit the wave–hull intersection, and it is different from the RANS grid in that, instead of high near-wall resolution, more points are distributed in the outer flow to resolve the wave field. The grid is 441×105 and consists of equal spacing in the axial direction and a power distribution

$$Y_{i,j} = (Y_{\text{body}} + 0.0002) + (1 - Y_{\text{body}})\left(\frac{j-1}{\text{jmax} - 1}\right)^n \quad (27)$$

in the transverse direction, where $n = 2$, jmax is number of points, and 0.0002 is an offset to ensure nonzero velocity. For regions upstream and downstream of the ship, $Y_{\text{body}} = 0$.

Communication between the RANS and free-surface grids is accomplished using bi-linear interpolation such that the velocity field from the ζ = kp1 plane of the RANS grid is interpolated to the free-surface grid. Similarly, the wave elevation is interpolated from the free-surface grid to the ζ = kp1 plane of the RANS grid.

Overall Solution Procedure

The overall solution algorithm is based on the pressure-implicit split-operator (PISO) algorithm, where the velocity and pressure fields are coupled through a two-step iterative procedure. In the first step, the momentum equations (6) are solved implicitly, using a tridiagonal algorithm and the method of lines and the pressure from the previous time step $(n-1)$ for an intermediate velocity field denoted by an asterisk:

$$\phi_P^* = \frac{1}{1 + C_P(C_U + C_D + R_{\text{eff}}/\Delta\tau)}[C_{NE}\phi_{NE}^* + C_{NW}\phi_{NW}^* + C_{SE}\phi_{SE}^* + C_{SW}\phi_{SW}^* + C_{EC}\phi_{EC}^* + C_{WC}\phi_{WC}^* + C_{NC}\phi_{NC}^* + C_{SC}\phi_{SC}^* + C_P(C_U\phi_U^* + C_D\phi_D^* + R_{\text{eff}}\phi_P^{n-1}/\Delta\tau - (S_\phi)_P)]. \quad (28)$$

For steady flow, convergence of (28) is not required; therefore, only several iterations are used.

The second step consists of subiterations. First, the pressure equation (7) is solved implicitly, using a tridiagonal algorithm and the method of lines and ϕ_p^* for an intermediate pressure denoted by an asterisk:

$$(E_d^{11} + E_u^{11} + E_n^{22} + E_s^{22} + E_e^{33} + E_w^{33})\hat{p}_P^* = E_d^{11}\hat{p}_D^* + E_u^{11}\hat{p}_U^* + E_n^{22}\hat{p}_{NC}^* + E_s^{22}\hat{p}_{SC}^* + E_e^{33}\hat{p}_{EC}^* + E_w^{33}\hat{p}_{WC}^* - \hat{D}^*. \quad (29)$$

For steady flow, convergence of (29) is not required; therefore, only several iterations are used. Second, the momentum equation (29) is solved explicitly using $\hat{p}^*$ for the momentum correction denoted by a double asterisk:

$$\phi_P^{**} = \frac{1}{1 + C_P(C_U + C_D + R_{\text{eff}}/\Delta\tau)}[C_{NE}\phi_{NE}^* + C_{NW}\phi_{NW}^* + C_{SE}\phi_{SE}^* + C_{SW}\phi_{SW}^* + C_{EC}\phi_{EC}^* + C_{WC}\phi_{WC}^* + C_{NC}\phi_{NC}^* + C_{SC}\phi_{SC}^* + C_P(C_U\phi_U^* + C_D\phi_D^* + R_{\text{eff}}\phi_P^{n-1}/\Delta\tau - (S_\phi)_P)]. \quad (30)$$

ϕ_P^{**} is then used to update $\hat{p}_P^*$. For steady flow, convergence of the second step is not required; therefore, only several subiterations between (29) and (30) are used. At the completion of the second step, $\hat{p}_P^*$ and ϕ_P^{**} are underrelaxed and become $\hat{p}_P^n$ and ϕ_P^n. Convergence is determined using the L_2 norms (residuals) of the solution variables between time steps (n) and ($n - 1$),

$$\text{RES}_\phi = \frac{\sum_{i=1}^{ip1}\sum_{j=1}^{jp1}\sum_{k=1}^{kp1}|\phi_{i,j,k}^n - \phi_{i,j,k}^{n-1}|}{ip1 * jp1 * kp1}, \quad (31)$$

where ϕ represents U, V, W, $\hat{p}$, or ζ and should ideally display three or four orders of magnitude drop for a converged solution.

CONDITIONS AND GRIDS

The conditions simulate the experiments; i.e., for low Fr, Fr = 0 and Re = 2×10^6, and for high Fr, Fr = 0.316 and Re = 4×10^6. Note that in the former case the experimental Fr = 0.16; however, free-surface effects are negligible, except near the bow. A partial view of the Fr = 0.316 RANS grid is shown in Fig. 1. For both Fr, the inlet, exit, and outer boundaries are located at $X = (-0.4, 2.0)$ and $r = 1$. The first grid points off the body surface are located in the range $Y^+ < 2$ (=Re $U_\tau Y_n$). The RANS grid sizes were: for Fr = 0, $90 \times 30 \times 20 = 54000$; and for Fr = 0.316, $180 \times 40 \times 30 = 216000$ and $360 \times 60 \times 30 = 648000$. In the latter case, although the grid number was increased by a factor of 3, the differences between its solution and the former were relatively small (e.g., 4% change in C_T). The free-surface boundary condition grid size was 460×100. The values of the time increment and underrelaxation factors for velocity and pressure are 0.01, 1, and 0.1. The code has been optimized for vector machines and has demonstrated performance of 150+ Mflops (millions of floating-point operations per second) on the CRAY C90. C90 CPU-time and memory requirements were about 0.35 h and 4 MW (megawords) for Fr = 0 and 16.7/5.6 h and 43/14.3 MW for the two Fr = 0.316 grids. In the latter cases, this corresponds to approximately 4.6×10^{-5} s/grid-point/global-iteration and increases by factors of about 14/5 and 29/10 in comparison with the interactive approach. The convergence criterion was that the residual (31) for all variables be about 10^{-4}, which was satisfied in about 500 and 2000 global iterations for Fr = 0 and 0.316. Additional global iterations indicated small oscillations (i.e., 2% C_T) with minimal reduction in the residuals.

Note that recent work with the method includes extensive verification analysis (iterative and grid convergence and order-of-accuracy studies) for both simple and practical geometries [9]. The status is as follows: the uncertainty in iterative convergence is about 2%, i.e., the same as the present results; the uncertainty in grid convergence is about 1–2%, i.e., better than the present results due to the use of somewhat finer grids; and order of accuracy's vary between about 1.5–2.5 depending on geometry and flow complexity.

RESULTS

Results are presented in Figs. 2–7 for both Fr = 0 and 0.316; however, the emphasis is on the latter. The discussions focus on comparisons with both the data and interactive approach based on all data locations (see Fig. 3 of [3]), although only representative results are shown. For brevity, in most cases, the data and interactive approach results are not reproduced, but rather, a similar format is used as in [2–4].

For Fr = 0 (Figs. 6–7), the general features of the Fr = 0.16 data are predicted; i.e., stagnation effects near the bow, thin boundary-layer development on the forebody, and rapid thickening of the boundary layer on the

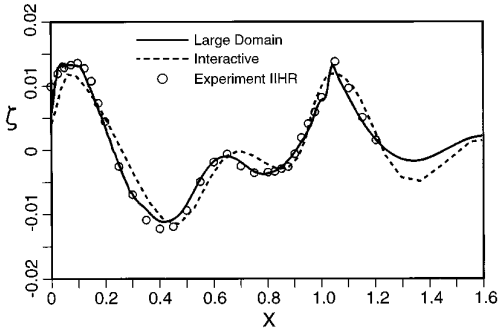

FIG. 2. Wave profiles.

afterbody with a characteristic bulge in the axial-velocity contours in the midgirth region and weak longitudinal vortex. Close to the hull and wake centerplane, improvement over [2] is indicated, due to the superior performance of the present Baldwin–Lomax near-wall turbulence model versus the previous k-ε turbulence model with wall functions. Apparently, the effects of near-wall modeling override zero versus two-equation differences. However, despite this improvement, the assessment is the same as [2]; i.e., significant improvements are required in the CFD development for detailed resolution of the viscous flow.

For Fr = 0.316, the wave profile (Fig. 2) shows overall close agreement with the data, including amplitude, shape, and phase; however, at the bow, the amplitude is underpredicted. Subsequent work has shown that this discrepancy is due to the inability of the CFD to simulate a thin film (about 1.5-mm thick) and bow vortex present at the bow of the Series 60 $C_B = 0.6$ ship model [11]. The wave-elevation and -slope contours (Fig. 3) also show similarity with the data, especially in the local region; however, differences are observed in the global region. The differences are highlighted by the transverse and longitudinal wave-elevation profiles (Fig. 4). In the former case (Fig. 4a), on the forebody, good agreement is indicated with both the local and global data, although the bow-wave crest and shoulder-wave trough are somewhat under and overpredicted. On the afterbody, good agreement is also indicated with the local data; however, as already noted, the complex global-region wave system is not replicated. In the latter case (Fig. 4b), the results are consistent, i.e., the amplitudes of the crests and troughs are underpredicted, especially in the global region. The discrepancies increase with distance from the hull. Improvement over [2] is indicated, especially for the wave profile and local-region wave system, due to the inclusion of nonlinear effects. Both approaches display a similar inability to predict the global-region wave system, which is unexpected due to the large methodological differences between the two approaches in this region.

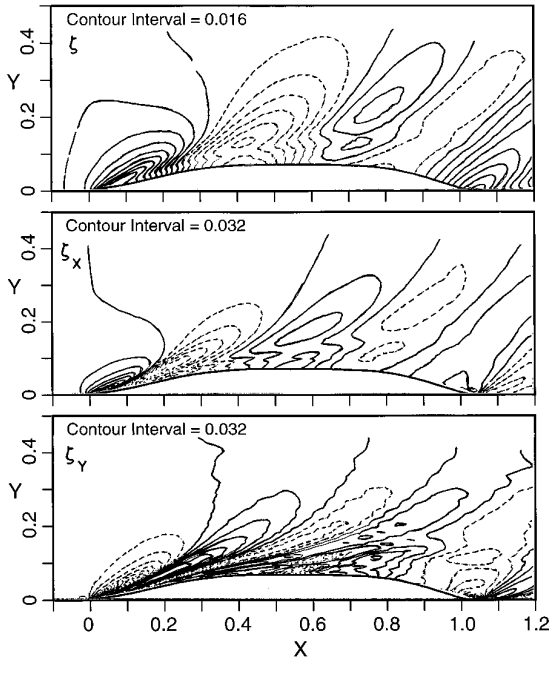

FIG. 3. Wave-elevation and wave-slope contours.

The surface pressure and gradient contours (Fig. 5) show good agreement with the data with regard to regions of positive and negative pressure and favorable and adverse pressure gradient. The results are similar to [2], except for nonlinear effects. The wall-shear stress contours (figure not shown) are consistent with expectation; however, no data is available for comparison. The value for the total resistance coefficient C_T was 5.79×10^{-3}, which is within 2% of the data ($C_T = 5.89 \times 10^{-3}$). Note that this percent difference is at about the accuracy of the data 0.5–5%. The value for the calculated pressure-resistance coefficient C_P was 2×10^{-3}, whereas the value for the experimental residuary-resistance coefficient C_R (i.e., $C_T - C_{F0}$) was 2.462×10^{-3} (i.e., −19% difference). The value for the frictional-resistance coefficient C_F was 3.8×10^{-3}, whereas the Schoenherr coefficient C_{F0} is 3.423×10^{-3} (i.e., 11% difference, which is equivalent to a form factor $k = 0.11$).

The mean-velocity and pressure field results (Figs. 6–7) show:

at $X = 0.0$, the general features of the stagnation effects displayed in the data. The U and $\hat{p}$ contours show close similarity to the data with respect to regions of low velocity and high pressure. The U contours are curved back toward the centerplane as is observed in the data. The velocity and pressure profiles show similar Fr differences and good agreement with the data, except that the V values are somewhat underpredicted, which may be due to lack of grid resolution with regard to finite-thickness effects. The U values are larger for Fr = 0.316, but the differences reduce with depth. The V profiles show small Fr differ-

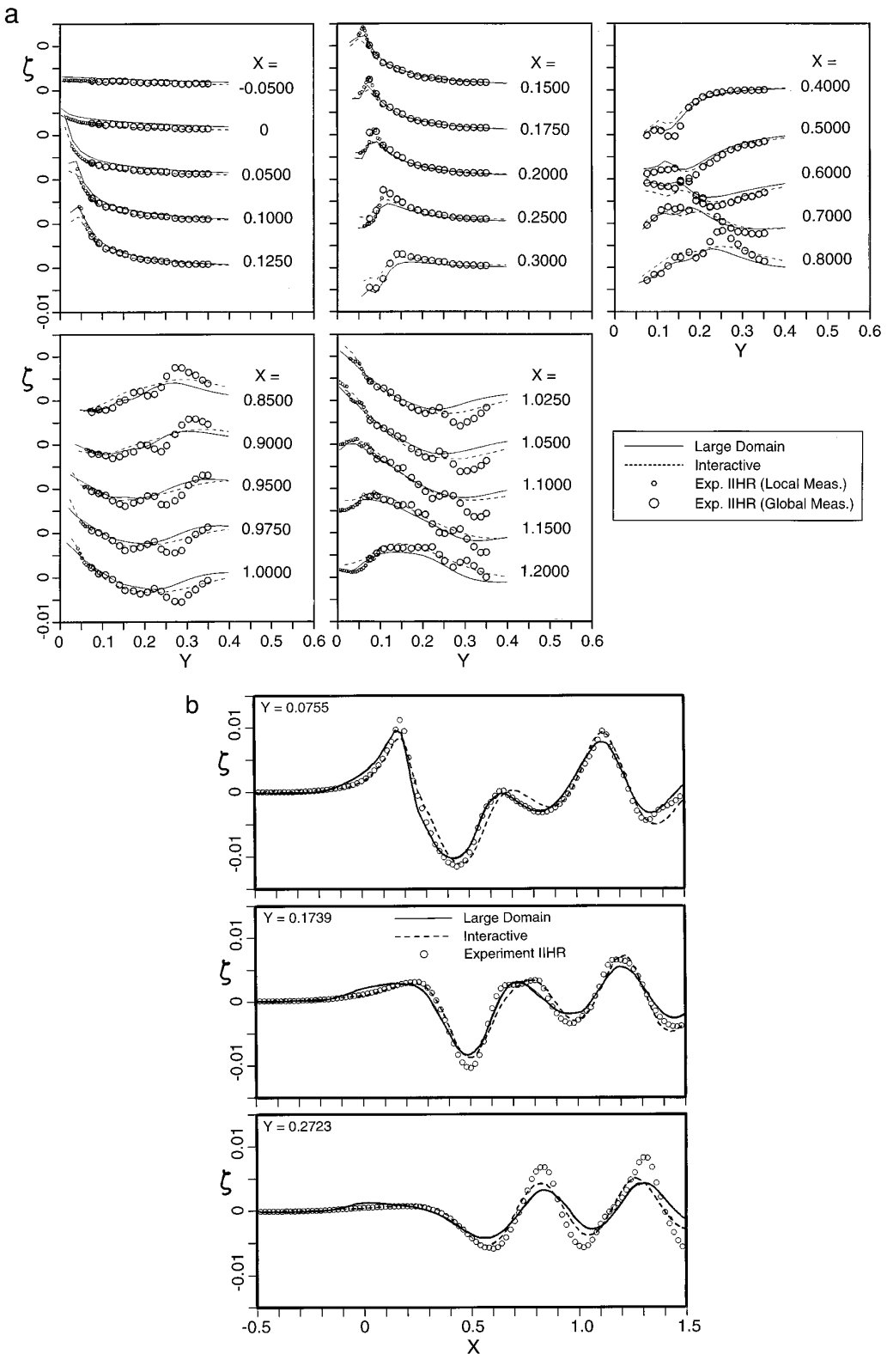

FIG. 4. Wave-elevation profiles: (a) Transverse; (b) Longitudinal.

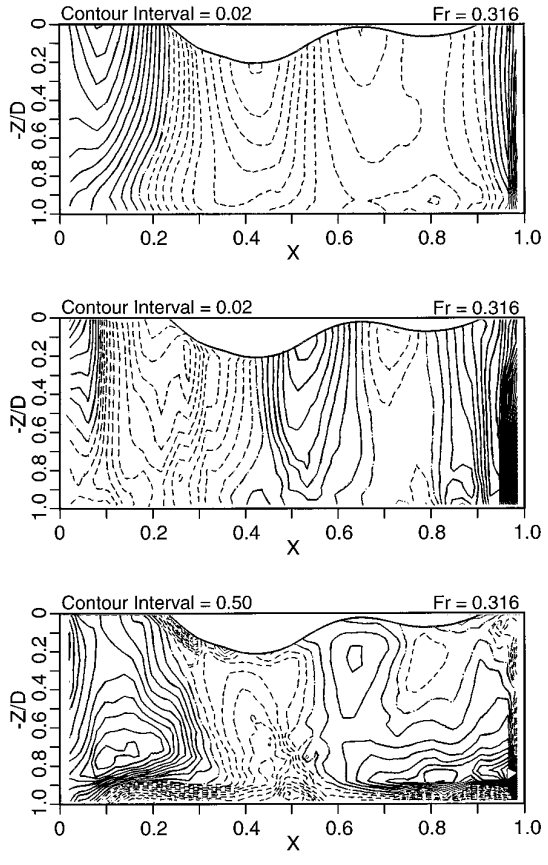

FIG. 5. Surface-pressure and gradient contours: Pressure (upper); Axial gradient (middle); Vertical gradient (lower).

ences, whereas the W values are larger for Fr = 0.316 for all depths. The $\hat{p}$ profiles are similar to the U profiles, but with a reverse trend in magnitude.

At X = (0.1, 0.2, 0.4), the free-surface effects on the thin boundary-layer development are simulated. The U contours are similar to the data with regard to the broad region of $U < 1$ at $X = 0.1$ and 0.2 and increased values in the outer region at $X = 0.4$. This is also true for the $\hat{p}$ contours regarding the broad region of high pressure at $X = 0.1$ and 0.2. At $X = 0.4$, the $\hat{p}$ contours show lower values for Fr = 0.316 and the contours are nearly parallel to the free surface as is observed in the data. The velocity and pressure profiles show similar trends to the data, including reduced Fr differences with depth. At $X = 0.1$ and 0.2, the U profiles indicate smaller values for Fr = 0.316, whereas these show larger values at $X = 0.4$. At $X = 0.1$ and 0.2, the V values are reduced and increased in the inner and outer regions. At $X = 0.4$, the V profiles show minimal Fr differences. At $X = 0.1$, the W profiles show reduced and increased values in the inner and outer regions, whereas they show reduced values overall at X = 0.2 and 0.4. These complex features of the flow are due to the formation of the bow-bilge vortex.

At X = (0.6, 0.8, 0.9), free-surface effects on the thick boundary-layer development are simulated. At $X = 0.6$, the U contours show reduced values in the outer region; and, at $X = 0.8$ and 0.9, the reduction in the boundary layer and more pronounced mid-girth bulge is observed for Fr = 0.316, which are also shown in the data. The $\hat{p}$ contours show similar trends to the data; i.e., the regions of increased and decreased values are reproduced. The formation of the stern-bilge vortex is reproduced, however, with smaller magnitude than the data. The velocity and pressure profiles show similar trends to the data. The Fr differences for these profiles penetrate to larger depths as is observed in the data. However, the V and W profiles generally have smaller predicted values in the inner region.

At X = (1, 1.1, 1.2), the free-surface effects on the wake development are simulated. The U and $\hat{p}$ contours show similarity to the data; however, they lack detail, especially near the core of the longitudinal vortex. The depthwise reduction in the boundary-layer thickness for Fr = 0.316 is observed in the U contours, as is the case for the data. The vectors show that the longitudinal vortex is shifted outward as is seen in the data; however, the magnitudes are underpredicted. The velocity and pressure profiles show similar trends to the data; however, some discrepancies are observed in the U profiles near the centerplane at larger depths. This is also true for the V and W profiles. These shortcomings are similar to those for Fr = 0. On the other hand, the $\hat{p}$ values show good agreement with the data. The results show improvement over [2] with regard to the resolution of the flow close to the hull and wake centerplane and of the Fr differences, due to near-wall turbulence modeling and nonlinear effects; however, detailed resolution of the viscous flow is still lacking.

CFD WORKSHOP TOKYO 1994

Recently, the *CFD Workshop, Tokyo 1994* [6] was held in Tokyo, Japan on March 22–24, 1994. The purpose of the workshop was to assess the state of the art of CFD for steady flow around ships and to accelerate further developments through discussion among the participants, in conjunction with comparisons of the computed results with each other and with the data. Previous related workshops were held on viscous flow in 1980 and 1990 [12, 13] and on inviscid flow in 1978, 1982, and 1987 [14–16]. Three test cases were used: (1) turbulent free-surface flow (Series 60 $C_B = 0.6$ ship model); (2) inviscid free-surface flow (Series 60 $C_B = 0.6$ ship model); and (3) turbulent double-model flow (HSVA ship models). Both the present large-domain and precursory interactive results were included in Test Case 1. Note that the data used presently [3, 4] was also used at the workshop for Test Cases 1 and 2.

In Test Case 3, 15 entries representing 7 nations participated. The CFD methods included both pseudo-compress-

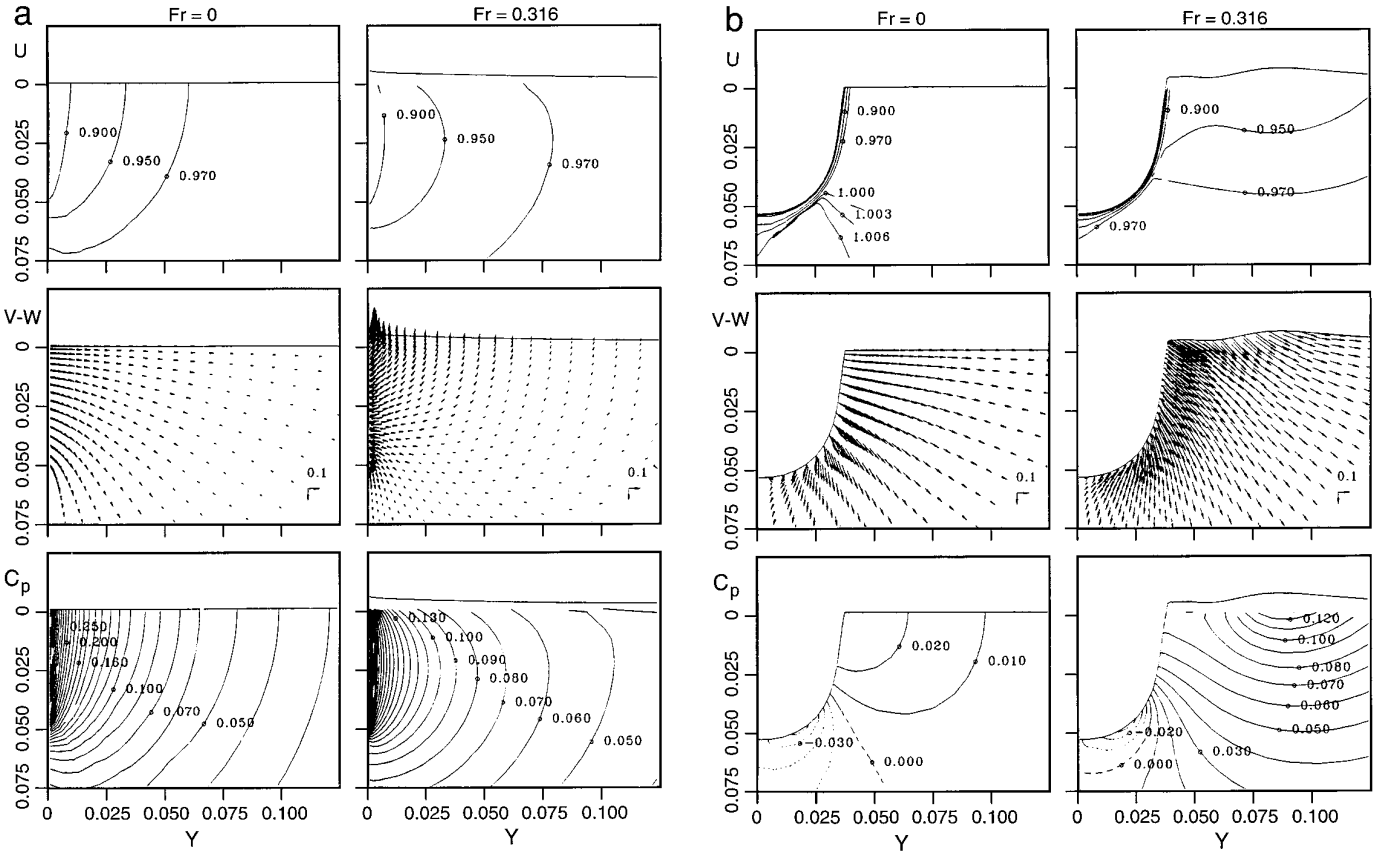

FIG. 6. Axial-velocity and pressure contours and crossplane vectors: (a) x = 0; (b) x = 0.2, (c) x = 0.6; (d) x = 0.9; (e) x = 1.1.

ibility and SIMPLER, PISO, and MAC types with first- and higher-order discretization procedures, simple and advanced grid-generation techniques, and isotropic (Cebici–Smith, Baldwin–Lomax, and k-ε) and nonisotropic (differential Reynolds-stress) turbulence models. The Baldwin–Lomax and k-ε models included the use of both wall functions and near-wall models and, in some cases, modifications for the present applications. Also, in one case, a very simplified subgrid scale model was used. The comparisons indicated that the nonmodified isotropic models were unable to produce the detailed flow pattern (e.g., hook-shaped axial-velocity contours near the stern), similarly as in the previous related workshop. The modified Baldwin–Lomax and k-ε models with near-wall models showed some improvement, but were insufficiently documented, including physical justification, to be considered generally useful. However, the differential Reynolds-stress models showed marked improvement, which confirms the necessity for nonisotropic turbulence models for the present applications. Also, higher-order discretization procedures and advanced grid-generation techniques indicated improvement.

In Test Case 2, eight entries representing seven nations participated. The CFD methods included potential and Euler types utilizing both linear and nonlinear free-surface boundary conditions. In many aspects, the inviscid-flow results showed remarkably good agreement with the data, including wave profile, surface-pressure distribution, and residuary resistance. However, the wave profiles indicated a downstream phase shift, the stern pressure rise and waves were overpredicted, the detailed wave pattern associated with the complex interactions of the bow, shoulder, and stern waves was not accurately resolved, especially the wave slopes, and the viscous effects were completely missing. The potential and Euler types showed similar results with the nonlinear methods indicating improvement; however, definitive general conclusions cannot yet be reached as to the differences between the potential versus Euler and linear versus nonlinear methods.

In Test Case 1, 11 entries representing 4 nations participated. The CFD methods were based on extensions of the types described for Test Case 3 for nonzero Fr calculations utilizing both linear and nonlinear approximate free-surface boundary conditions and interactive and large-domain approaches. In comparison to Test Case 3, relatively fewer methods were able to obtain satisfactory results. Both ap-

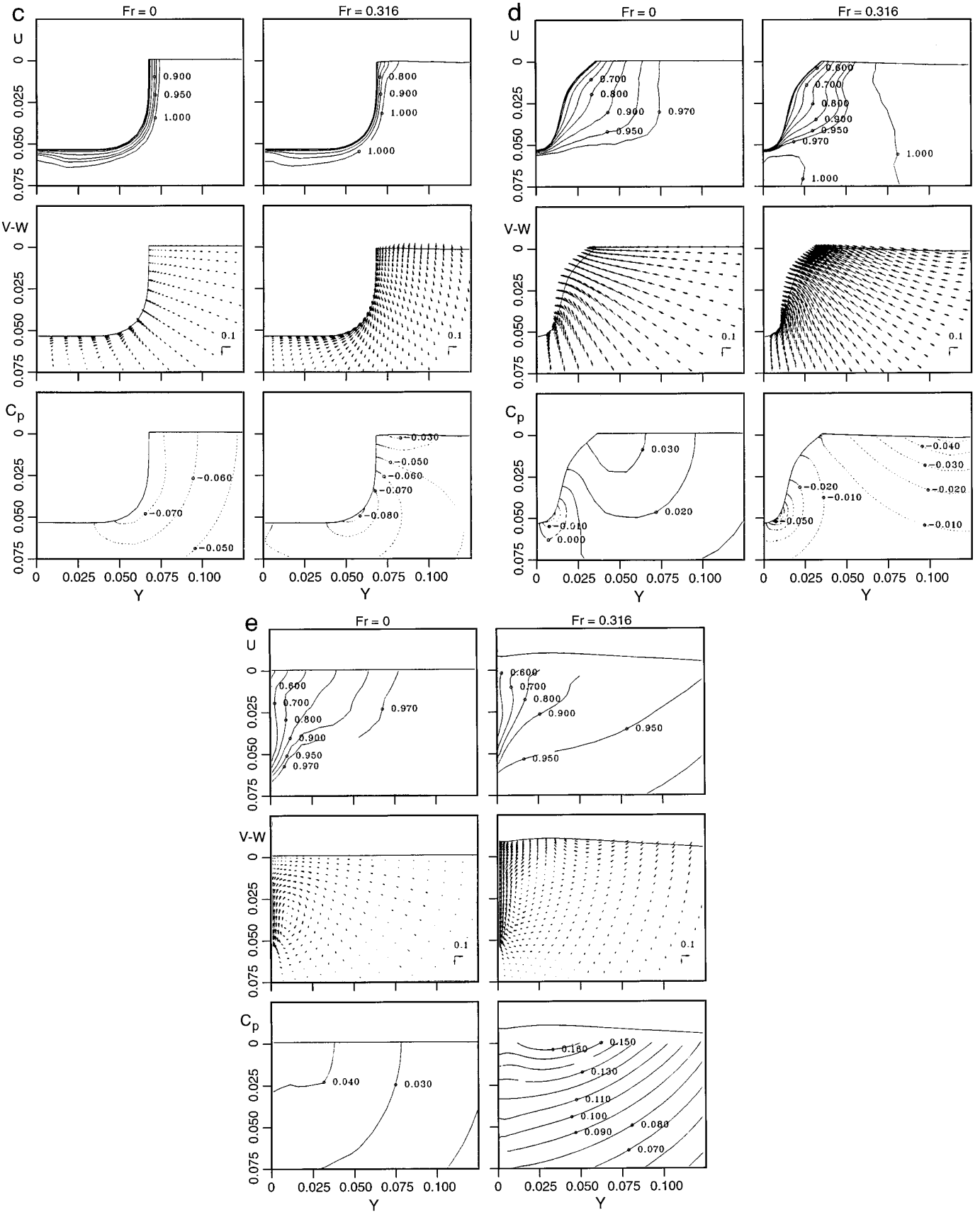

FIG. 6—*Continued*

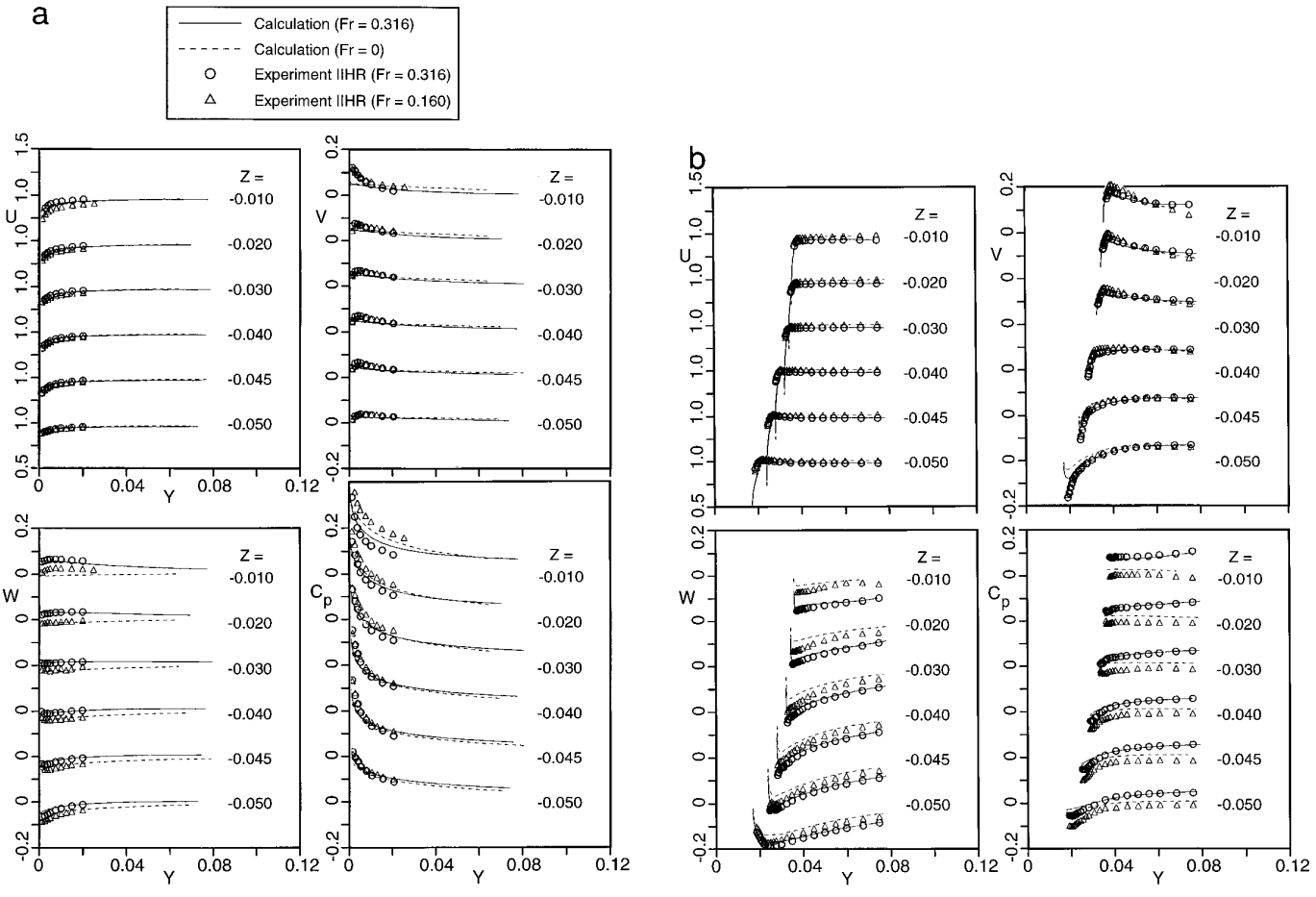

FIG. 7. Velocity and pressure profiles: (a) x = 0; (b) x = 0.2; (c) x = 0.6; (d) x = 0.9; (e) x = 1.1.

proaches showed similar results with regard to free-surface effects as described for Test Case 2, but with significant improvement for the wave profile phase, stern pressure rise and waves, and the presence of viscous effects. The resistance values were at about the accuracy of the data. Also, viscous effects for the Series 60 $C_B = 0.6$ ship model for nonzero Fr are similar to those for zero Fr, but with wave-induced pressure gradient effects, such that the conclusions with regard to Test Case 3 are also valid for Test Case 1.

In all three test cases, the entries showed varying capabilities and, in many cases, their procedures were insufficiently documented. In particular, limited verification analysis (i.e., iterative and grid convergence and order of accuracy studies) was provided. The previous discussion was based on the best quality entries, which, in Test Case 1, included both the present large-domain and precursory interactive approaches. The workshop was successful with the conclusion that the status of CFD for ship hydrodynamics is such that the predicted steady resistance and flow are nearly at the accuracy of the experimental data. However, certain detailed flow features of the wave pattern and viscous flow are inadequately resolved, indicating the need for improvements in numerical accuracy, turbulence modeling (e.g., use of nonisotropic turbulence models), grid generation, and treatment of the free-surface boundary conditions. Nonetheless, the status suggests that the better methods will be useful for design applications. The results from such applications should also be useful in aiding improvements, which are expected to follow in conjunction with extensions for more complex flows.

CONCLUDING REMARKS

A large-domain approach is developed for calculating ship boundary layers and wakes and wave fields for nonzero Fr. The RANS and continuity equations are solved with the Baldwin–Lomax turbulence model, exact nonlinear kinematic and approximate dynamic free-surface boundary conditions, and a body/free-surface conforming grid. The results are validated through comparisons with data for the Series 60 $C_B = 0.6$ ship model at low and high

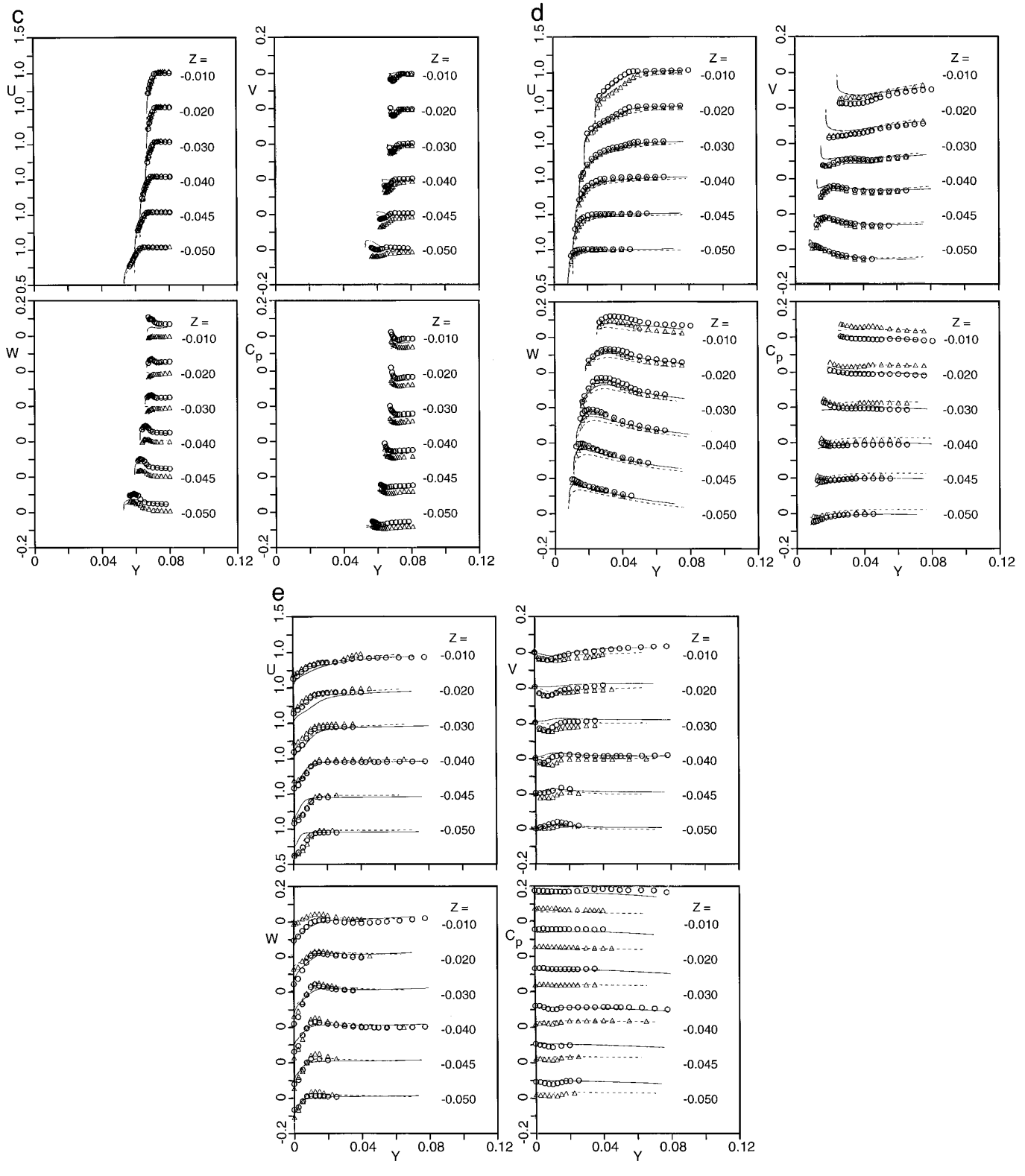

FIG. 7—*Continued*

Fr and results of the precursory interactive approach. Both approaches yield satisfactory results; however, the large-domain results indicate improved resolution of the flow close to the hull and wake centerplane and of the Fr differences due to near-wall turbulence modeling and nonlinear free-surface boundary conditions. Both methods were among the best at the recent *CFD Workshop, Tokyo 1994* [6].

Although both approaches accurately predict the general features of the flow, detailed resolution is lacking both for the wave field and viscous flow. For the interactive approach, improvements require inclusion of nonlinear effects and in CFD development. Based on [17], the former is not expected to significantly improve the detailed predictions. For the large-domain approach, improvements require development of procedures for more accurate imposition of the free-surface boundary conditions, including inclusion of viscous and turbulence effects and in CFD development. Based on [18], the viscous terms are expected to have a significant influence close to the free surface in regions of large velocity and wave gradients. Improvements in CFD development require advancements in higher-order discretization procedures, turbulence modeling, and grid generation.

As already noted, improvements in CFD development are expected to follow in conjunction with extensions for more complex flows. For example, recent work with the present method includes extensions for unsteady flow with application to wave-induced separation for a surface-piercing NACA 0024 foil over a range of Fr [19] and for the inclusion of thermal-stratification and two-fluid modeling with application to near- and far-field flows for naval combatants [20]. Hopefully, through such extensions and applications, in conjunction with verification, validation, and calibration methods such as the present one, will be accredited as engineering tools for future designs.

ACKNOWLEDGMENTS

This research was sponsored by the Office of Naval Research Grant N00014-92-1092 under the administration of Dr. E. P. Rood. The computations were performed on the Army Waterways Experiment Station and National Aerodynamic Simulation Program supercomputers. Dr. E. G. Paterson is gratefully acknowledged for his help in preparing the manuscript.

REFERENCES

1. Y. Tahara, F. Stern, and B. Rosen, *J. Comput. Phys.* **98**(1), 33 (1992).
2. Y. Tahara and F. Stern, *J. Comput. Fluids* **23**(6), 785 (1994).
3. Y. Toda, F. Stern, and J. Longo, *J. Ship Res.* **37**(4), 360 (1992).
4. J. Longo, F. Stern, and Y. Toda, *J. Ship Res.* **37**(1), 16 (1993).
5. F. Stern, S. Y. Yoo, and V. C. Patel, *AIAA J.* **26**(9), 1052 (1988).
6. *Proceedings, CFD Workshop Tokyo, Ship Research Institute Ministry of Transport Ship & Ocean Foundation, 22–24 March 1994,* Vols. 1, 2.
7. H. C. Chen and V. C. Patel, "The Flow around Wing-Body Junctions," in *4th Sympos. Numer. Phys. Aspects Aerodyn. Flows, Long Beach, CA, 1989* (unpublished).
8. H. C. Chen and V. C. Patel, *J. Comput. Phys.* **88**(2), 305 (1990).
9. F. Stern, E. G. Paterson, and Y. Tahara, IIHR Report, IIHR, University of Iowa, Iowa City, Iowa, 1996 (in preparation).
10. F. Stern, H. T. Kim, D. H. Zhang, Y. Toda, J. Kerwin, and S. Jessup, *J. Ship Res.* **38**(2), 137 (1994).
11. F. Stern, J. Longo, and Z. J. Zhang, "Detailed Bow-Flow Data and CFD of a Series 60 CB = .6 Ship Model for Froude Number .316," in *Proceedings, 24th ATTC, College Station, Texas, November 1995* (unpublished).
12. L. Larsson, SSPA Publication No. 90, 1981.
13. L. Larsson, V. C. Patel, and G. Dyne, Flowtech International Report No. 2, June 1991.
14. K. J. Bai and J. H. McCarthy, *Proceedings, Workshop on Ship Wave Resistance Computations* (DTNSRDC, Bethesda, MD, 1979).
15. F. Noblesse and J. H. McCarthy, *Proceedings, Second Workshop on Ship Wave Resistance Computations* (DTNSRDC, Bethesda, MD, 1983).
16. W. T. Lindenmuth, T. J. Ratcliffe, and A. M. Reed, Technical Report DTRC/SHD-1260-01, David Taylor Research Center, 1988 (unpublished).
17. H. C. Raven, "Nonlinear Ship Wave Calculations Using RAPID Method," in *Proceedings, Sixth International Conf. on Numerical Ship Hydrodynamics, Iowa City, Iowa, August 1993,* p. 95.
18. J. E. Choi and F. Stern, "Solid–Fluid Juncture Boundary Layer and Wake with Waves," in *Proceedings, Sixth International Conf. on Numerical Ship Hydrodynamics, Iowa City, Iowa, August 1993,* p. 215.
19. Z. Zhang and F. Stern, "Wave-Induced Separation," in *ASME Forum on Advances in Numerical Modeling of Free Surface and Interface Fluid Dynamics, San Francisco, CA, 12–17 November 1995* (unpublished).
20. E. G. Paterson and M. C. Hyman, F. Stern, P. A. Carrica, F. Bonneto, and D. Drew, "Near- and Far-Field CFD for Naval Combatants Including Thermal Stratification and Two-Fluid Modeling," in 21st ONR Symposium on Naval Hydrodynamics, Trondheim, Norway, June 1996 (unpublished).